Magnesiophilic Graphitic Carbon Nanosubstrate for Highly Efficient and Fast-Rechargeable Mg Metal Batteries

Hee-Dae Lim,*,† Dae Hyun Kim,†,‡ Sunwoo Park,§ Min Eui Lee,‖ Hyoung-Joon Jin,§ Seungho Yu,† Si Hyoung Oh,† and Young Soo Yun*,⊥,#

†Center for Energy Storage Research, Korea Institute of Science and Technology (KIST), Hwarang-ro 14-gil 5, Seongbuk-gu, Seoul 02792, South Korea

‡Department of Materials Science and Engineering, Seoul National University of Science and Technology, Seoul 139-743, South Korea

§Department of Polymer Science and Engineering, Inha University, Incheon 22212, South Korea

‖Carbon Composite Materials Research Center, Institute of Advanced Composite Materials, Korea Institute of Science and Technology, 92 Chudong-ro, Bongdong-eup, Wanju-gun, Jeollabuk-do 55324, South Korea

⊥Department of Chemical Engineering, Kangwon National University, Samcheok 25913, South Korea

#KU-KIST Graduate School of Converging Science and Technology, Korea University, 145 Anam-ro, Seongbuk-gu, Seoul 02841, South Korea

S *Supporting Information*

ABSTRACT: The high volumetric energy density of rechargeable Mg batteries (RMBs) gives them a competitive advantage over current Li ion batteries, which originates from the high volumetric capacity (∼3833 mA h cm^{-3}) of bivalent Mg metal anodes (MMAs). On the other hand, despite their importance, there are few reports on research strategies to improve the electrochemical performance of MMAs. This paper reports that catalytic carbon nanosubstrates rather than metal-based substrates, such as Mo, Cu, and stainless steel, are essential in MMAs to improve the electrochemical performance of RMBs. In particular, three-dimensional macroporous graphitic carbon nanosubstrates (GC-NSs) with high electrical conductivities can accommodate Mg metal with significantly higher rate capabilities and Coulombic efficiencies than metal substrates, resulting in a more stable and longer-term cycling performance over 1000 cycles. In addition, while metal-based substrates suffered from undesirable Mg peeling-off, homogeneous Mg metal deposition is well-guided in GC-NSs owing to the better affinity of the Mg^{2+} ion. These results are supported by density functional theory calculations and ex-situ characterization.

KEYWORDS: nanosubstrate, carbon substrate, magnesiophilic, metal anode, Mg battery
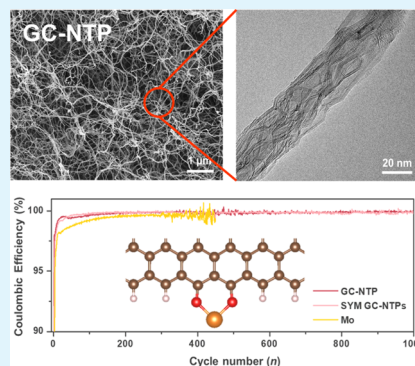
INTRODUCTION

One of the major global issues is the development of more energetic power sources, enabling portable mobile electronics and electric vehicles with longer lifetimes and higher current and power densities. Rechargeable Mg batteries (RMBs) have attracted considerable attention, owing to the high theoretical volumetric capacity (∼3833 mA h cm^{-3}) of bivalent Mg metal, which is approximately 1.9 times higher than that of Li metal (2046 mA h cm^{-3}).[1−4] In addition, the bio-abundant and relatively nontoxic Mg metal has been reported to be free from dendritic metal growth, allowing it to be more reversible for electrochemical deposition/dissolution cycles.[1,5,6] The host-free Mg metal anode (MMA) can deliver an unlimited capacity and has a high rate capability, whereas the absence of an applicable electrolyte system has been a major issue for the MMA. In particular, conventional electrolytes that are used widely for lithium ion batteries, such as carbonate- or ether-based solvents with the combination of TFSI$^-$ and PF$_6^-$ salts, form passivation layers (i.e., non-ion-conductive layers) on the Mg metal surface.[6−10] These unwanted layers inhibit the transport of Mg ions at the interface between the electrode and electrolyte, where the blocked ionic pathways strongly deteriorate the Coulombic efficiencies (CEs) of RMBs, resulting in a poor cycling performance. To address this issue, electrolytes based on Grignard reagents (RMgX, R = alkyl or aryl group and X = Cl or Br) have been developed. Although strong reducing agents could prevent the formation of passivation on the Mg surface,[11,12] their practical applications have been hindered by its poor anodic stability. A decade later, Aurbach et al. developed a new electrolyte
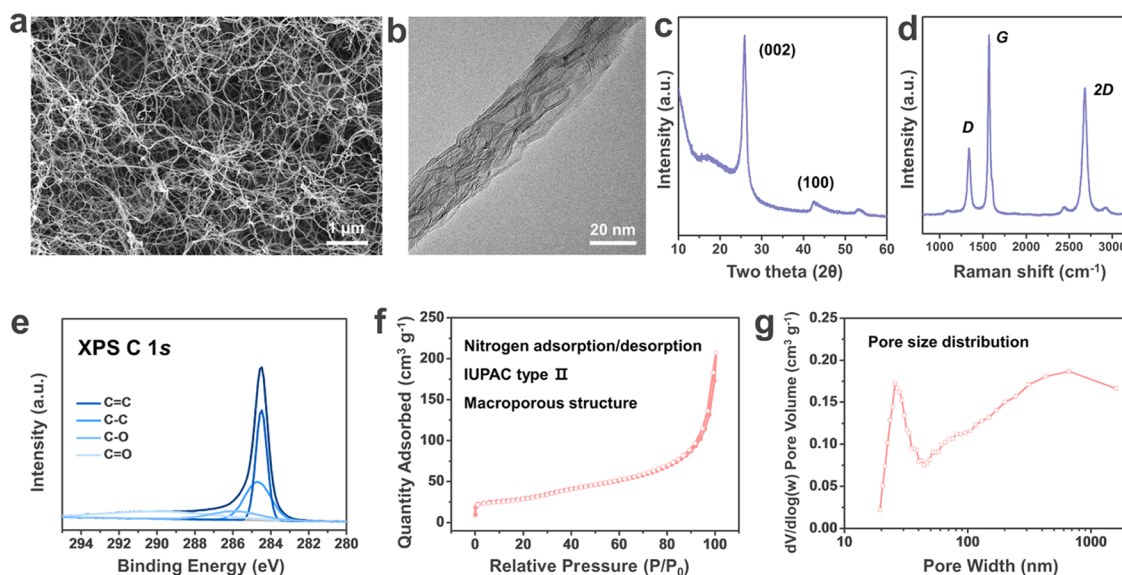
Figure 1. Material properties of GC-NSs: (a) FE-SEM image, (b) FE-TEM image, (c) XRD pattern, (d) Raman spectrum, (e) XPS C 1s spectrum, (f) nitrogen adsorption/desorption isotherm curve, and (g) pore size distribution data of GC-NSs.

system with improved anodic stability by mixing MgRR′ (R and R′= ethyl and butyl) and aluminum Lewis acid (e.g., $Bu_2Mg + AlCl_3$), and they demonstrated its practicability on RMBs.[13] Nevertheless, chloride-based compounds are corrosive to common current collectors as well as packaging materials.[14,15] Therefore, despite the strenuous efforts over the past several decades, finding a suitable electrolyte for MMA is still a challenge. Furthermore, the overall electrochemical performance of RMBs needs to be improved before they can substitute current Li-ion batteries, requiring a range of research strategies and attempts to secure the competitiveness of RMBs.

Although there has been relatively less research interest in the development of an anode system for RMBs, renewed interest has prompted studies on an efficient anode system. For example, MMA was coated with a carbon-based artificial interface layer to prevent direct contact between the Mg metal and electrolyte.[16] This results in highly reversible Mg metal deposition/stripping cycles in a conventional carbonate-based electrolyte system. On the other hand, the MMA has also been confronted by other important obstacles. The internal short circuit caused by the poor wettability of the electrochemically generated Mg on the Mg substrate needs to be resolved.[17] In addition, the unexpected dendritic growth under abnormal conditions needs to be considered[17,18] because it has gone unnoticed owing to the incomplete knowledge in this field. Even with the use of Grignard reagents in a symmetric Mg—Mg cell, the formation of Mg dendrites was observed recently.[18] These problems could be alleviated somewhat using other types of anode materials (i.e., alloying-/conversion-type materials[19–22]). However, the development of a highly reversible MMA would be a key to achieving high-performance RMBs considering that the high volumetric energy density of RMBs can be achieved only when MMAs are applied rather than alloy-type or conversion-based anode materials. Despite this, there has been little improvement in the electrochemical performance of MMAs, such as their rate capabilities, Coulombic efficiency (CE), and cycling stability. In addition, few studies have examined ways of mitigating dendritic metal growth.

This paper reports a new research strategy with a catalytic carbon nanosubstrate in MMAs. As a modeled carbon structure, three-dimensional macroporous graphitic carbon nanosubstrates (GC-NSs) composed of graphitic carbon nanofibers (GC-NFs) were fabricated to operate MMAs efficiently for RMBs. Freestanding GC-NSs can be used without heavy-metal-based substrates by simply punching them to the desired size, resulting in enhanced energy densities. In addition, the specific open surface area, which is 1000 times higher than those of flat metal foils, and the favorable absorption for Mg^{2+} ions could be due to the reduced nucleation polarization and improved rate capabilities. The numerous catalytic edges of graphitic carbon are advantageous for Mg absorption, leading to an efficient metal plating/dissolution process. These results show that carbon nanosubstrates are indispensable for achieving high-performance MMAs.

■ RESULTS AND DISCUSSION

As catalytic carbon nanosubstrates for efficient RMBs, stereoscopic morphologies were designed for GC-NSs, as shown in Figure 1a. High-aspect-ratio GC-NFs were entangled three-dimensionally to form a complex network structure, including numerous macropores, a few micrometers in width (Figure 1a). The respective fiber diameters and lengths were ~25 nm and >10 μm. The graphitic microstructure of GC-NFs observed by field-emission transmission electron microscopy (FE-TEM) exhibited an interesting shape in that several two-dimensional graphitic lattices were twisted three-dimensionally (Figure 1b). The graphitic microstructures can expose a number of graphitic edge sites into the open surface, extending the catalytic sites for Mg metal nucleation. The X-ray diffraction (XRD) pattern of GC-NSs proved the well-developed graphitic crystal structure, where a sharp graphite (002) peak was observed at 25.9° 2θ with smaller graphite (100) and (004) peaks at 43 and 54° 2θ, respectively (Figure 1c). In addition, the Raman spectrum revealed further specific microstructural information (Figure 1d). A sharp G band at 1573 cm^{-1} had more than double the intensity of the D band at 1340 cm^{-1}, indicating the presence of well-developed poly-
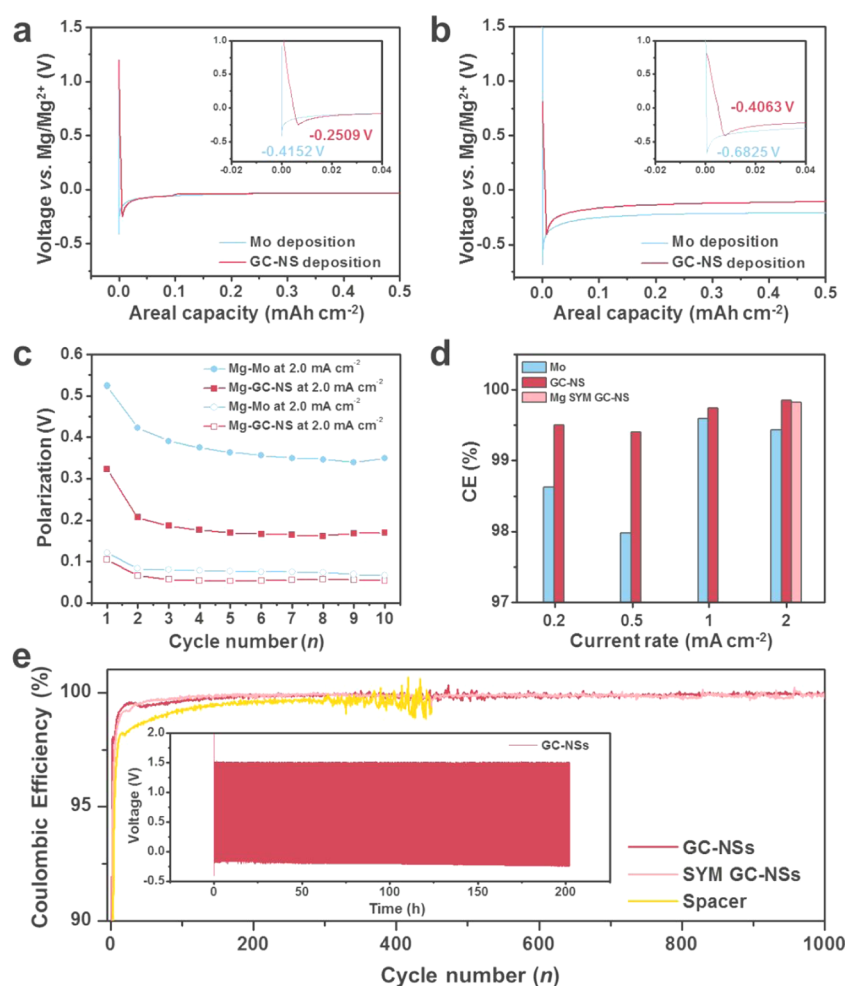
Figure 2. Electrochemical performance of the GC-NS-Anode and Mo-Anode in an all-phenyl complex electrolyte. Galvanostatic Mg metal deposition at current rates of (a) 0.2 mA cm^{-2} and (b) 2 mA cm^{-2}. Comparisons of the (c) voltage hysteresis of Mg plating/stripping at the initial 10 cycles, (d) current rate vs CE relationships from 0.2 to 2 mA cm^{-2}, and (e) cycling behaviors (the inset is a time vs voltage plot of the GC-NS-Anode).

hexagonal carbon structures. Moreover, the high-intensity 2D band at 2688 cm^{-1} indicated that the carbon structure had three-dimensional ordering (Figure 1d). The surface chemical structure of the GC-NSs was observed by X-ray photoelectron spectroscopy (XPS) (Figure 1e). In the XPS C 1s spectrum, the main chemical bonding of GC-NSs was confirmed to be sp^2 C=C bonding at 284.4 eV. In addition, sp^3 C—C bonding with a high intensity was also observed at 284.8 eV, which could originate from the edge defects of polyhexagonal carbon building blocks. One of the noteworthy results is the presence of oxygen functional groups, such as C—O and C=O at 285.6 and 289.9 eV, respectively. These oxygen groups could improve the wettability of the hydrophobic graphitic building blocks in the hydrophilic electrolyte system. The porous properties of GC-NSs were characterized by nitrogen adsorption and desorption isotherm tests (Figure 1f,g). The isotherm curve exhibited a dramatic increase in the quantity of adsorbed nitrogen molecules in a >0.9 section of relative pressure, indicating an International Union of Pure and Applied Chemistry type-II, macroporous structure (Figure 1f). This coincides with the field-emission scanning electron microscopy (FE-SEM) result shown in Figure 1a. The pore size distribution revealed a mean pore volume of approximately 20−30 nm along with several others that were hundreds of

nanometers in size (Figure 1g). The approximately 20−30 nm-sized pores could be induced by nitrogen adsorption on the surface of the respective fibers, whereas the larger ones could originate from the pores made by the nanoweb structure. The specific Brunauer−Emmett−Teller surface area of the GC-NSs was ~105.3 m^2 g^{-1}, which is much higher than those of flat metal substrates.

Electrochemical Mg deposition tests on GC-NS-based MMAs (GC-NS-Anode) and Mo substrate-based MMAs (Mo-Anode) were processed using the all-phenyl complex (APC) electrolyte (i.e., 0.5 M AlCl$_3$ + 2.0 M PhMgCl in tetrahydrofuran (THF)) (Figure 2a). The galvanostatic discharge profiles of both the GC-NS-Anode and Mo-Anode showed a voltage overshoot (VO) at the initial deposition step, which could indicate nucleation polarization (η_n).[23] According to the classical metal nucleation theory, the formation of a new solid phase requires surplus free energy to overcome a nucleation energy barrier, which is exhibited as the VO in the galvanostatic discharge profile. The initial nucleation overpotential of the Mo-Anode (~0.42 V) can be reduced significantly using GC-NSs to ~0.25 V, corresponding to ~60% of the reduction from the Mo-Anode at a moderate current density of 0.2 mA cm^{-2} (Figure 2a). The nucleation polarization becomes significant as the current density was
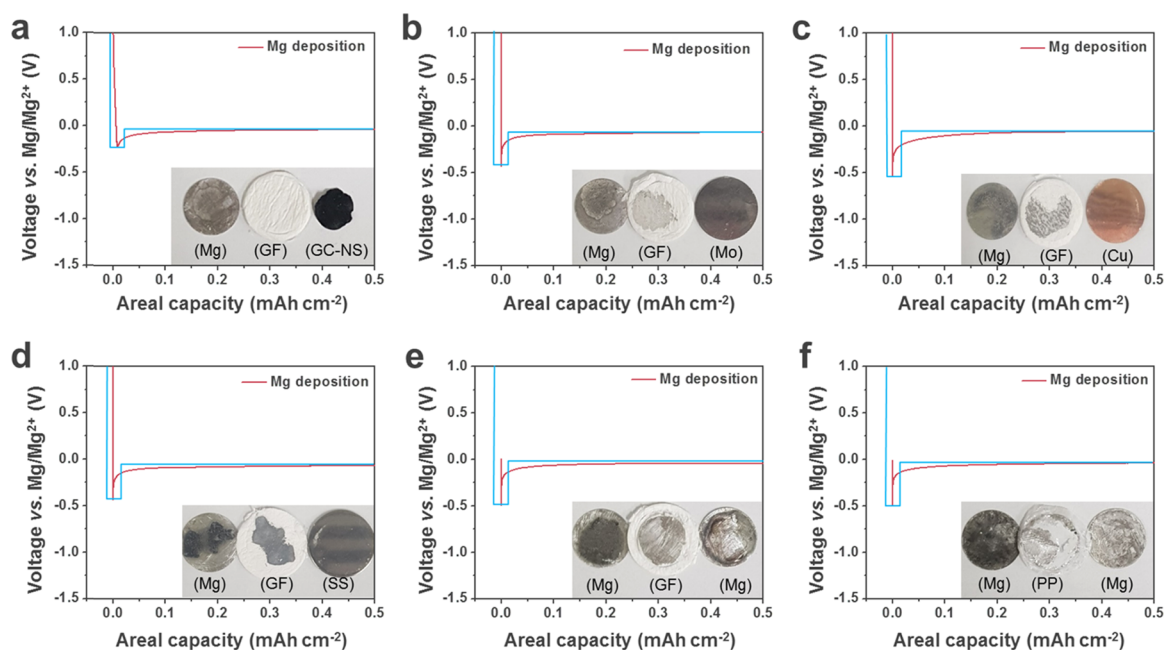
Figure 3. Comparison of the nucleation polarization for Mg plating on different substrates, such as (a) GC-NS, (b) Mo, (c) Cu, (d) SS, (e) Mg metal with a GF separator, and (f) for Mg plating on Mg metal with a polypropylene separator. The insets of each figure show the ex situ cell components after Mg deposition by an areal capacity of 5 mA h cm^{-2} at a current rate of 0.2 mA cm^{-2}.

increased (Figure 2b), and the gaps of the nucleation overpotentials between the two were broadened, reaching 0.27 V at a high current density of 2.0 mA cm^{-2}. The Supporting Information provides detailed electrochemical curves (Mg plating and stripping) for both the Mo-Anode and GC-NS-Anode at various current rates (0.2, 0.5, 1.0, and 2.0 mA cm^{-2}) (Figures S1 and S2). Therefore, the nucleation overpotentials as well as dendritic growth would be more problematic at high current rates, and the GC-NS-Anode could be a solution for alleviating the problems.

The overpotentials originating from ohmic polarization (i.e., plateau overpotential (η_p)) could also be reduced using the GC-NS-Anode. The GC-NS-Anode delivered a much lower plateau overpotential as well as a voltage hysteresis gap compared to the Mo-Anode, which could be observed clearly at a high current rate of 2.0 mA cm^{-2} (Figure 2b). Figure 2c presents the voltage hysteresis gap (denoted as polarization in the y-axis) of each cycle for the GC-NS-Anode and Mo-Anode at two different current rates of 0.2 and 2.0 mA cm^{-2}. Similar to the results of nucleation polarization, the difference in their voltage hysteresis became more significant with increasing current rates. While the difference in the average polarization in the initial 10 cycles showed only a 0.018 V gap at a relatively mild current rate of 0.2 mA cm^{-2}, a huge gap of ~0.192 V was observed at a high current rate of 2.0 mA cm^{-2}, which is an approximately 10 times higher polarization, producing significant energy loss (Figure 2c). Figure S3 also compares the average plateau overpotentials under different current rates. These results suggest that the kinetic performance, including the nucleation and ohmic polarization of a bivalent Mg metal deposition/dissolution process, is strongly dependent on a host for Mg ions. Therefore, a state-of-the-art anode, such as the GC-NS-Anode, might be advantageous when designing high-rate-performance RMBs.

The reductions of both the nucleation overpotential (η_n) and plateau overpotential (η_p) in the GC-NS-Anode can be explained in three ways. First, the high surface area of the GC-NS-Anode can reduce the effective current density at a given current rate, decreasing the overall resistance. Supposing that 1 mg of GC-NSs are used as the anode material, they can provide an approximately 1000 times higher specific active surface area for deposited Mg metal than the Mo-Anode. Considering the much lower bulk density of GC-NSs (~0.53 g cm^{-3}) than those of Mo (10.3 g cm^{-3}), Cu (~8.96 g cm^{-3}), stainless steel (SS, ~8.0 g cm^{-3}), and Al (2.7 g cm^{-3}), the GC-NS-Anode-based RMBs can deliver much higher specific energy densities and have higher power capabilities than the Mo-, Cu-, SS-, and Al-Anode-based RMBs. We chose Mo as a stable substrate in Mg batteries using chloride-complexed electrolytes, and Cu, SS, and Al as the typical current collectors in conventional Li-ion batteries. Second, the three-dimensionally entangled nanoweb structure with a high electrical conductivity of ~250 S cm^{-1} and numerous macropores can supply well-developed electrons and ion transport pathways, enabling efficient Mg metal deposition/dissolution on the internal macropores of the GC-NSs. These two effects would explain the much reduced plateau overpotential (η_p) of the GC-NS-Anode compared to that of the Mo-Anode. Third, the multitudinous catalytic sites of the GC-NS-Anode could provide numerous active sites for the nucleation of Mg metal, resulting in a reduced nucleation overpotential (η_n). The catalytic sites in the GC-NS-Anode help alleviate the overshooting voltage upon the initial Mg deposition, as shown in Figure 2. They can favorably absorb and accommodate Mg ions, showing a reduced overpotential for the initial deposition, which is supported by the density functional theory calculation results in Figure 4.

The high reversibility of the Mg metal deposition/dissolution cycles was confirmed by calculating the average CEs of the 10th−100th cycles at different current rates for both the GC-NS-Anode and the Mo-Anode (Figure 2d). At a current rate of 0.2 mA cm^{-2}, the GC-NS-Anodes showed an
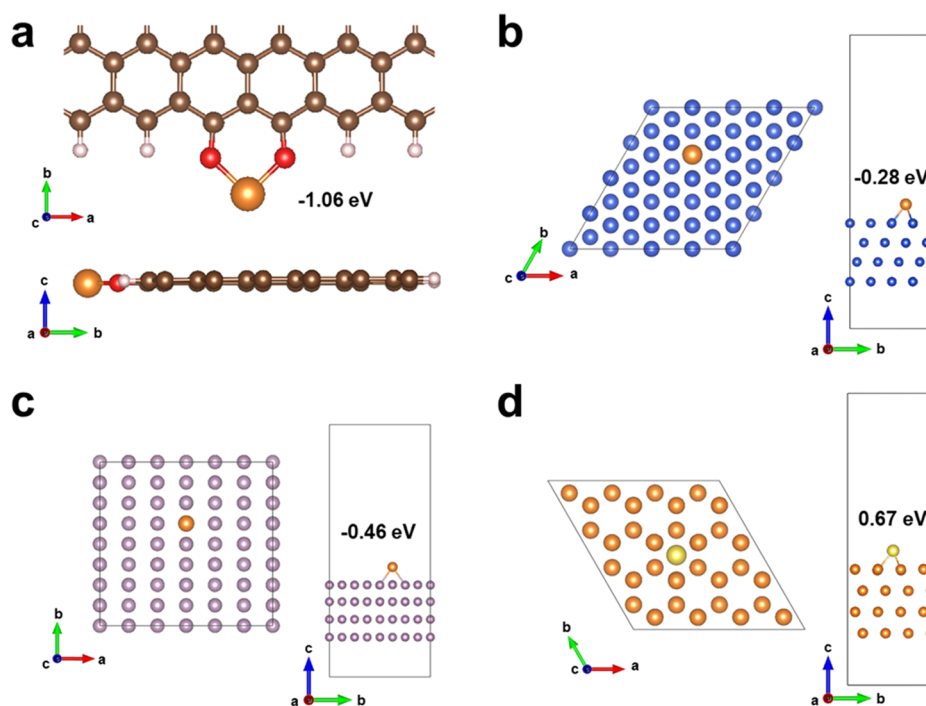
Figure 4. Relaxed configurations of Mg adsorption on (a) graphene terminated with hydrogen and oxygen, showing the view normal to the graphene sheet and along the graphene sheet. The lowest surface energy slabs and relaxed configurations of Mg adsorption on (b) Cu(111), (c) Mo(110), and (d) Mg(0001). Cu, Mo, and Mg atoms are colored blue, pink, and orange, respectively.

average CE value of ~99.6%, which increased gradually with increasing current rates and reached ~99.9% at current densities ≥2.0 mA cm^{-2}. In addition, the symmetric GC-NS-Anodes (SYM-GC-NS), which were assembled as a symmetric electrode configuration and Mg metal attached under one side of the electrode, showed a high CE value of ~99.9% at 2.0 mA cm^{-2}. In contrast, the Mo-Anodes exhibited slightly lower average CE values of ~99.1% at 0.2 mA cm^{-2}, which reached a maximum value of ~99.6% at 1.0 mA cm^{-2}. If 100 repetitive cycles are progressed by average CEs of 99.9% $[(0.999)^{100}]$, ~90.5% of the initial capacity could be retained after 100 cycles. On the other hand, only ~67.0% of the initial capacity could be maintained after 100 cycles from average CEs of 99.6% $[(0.996)^{100}]$. This suggests that the slight decrease in CE results in a tremendous decrease in capacity, highlighting the superior reversibility of the GC-NS-Anodes. For both the GC-NS- and symmetric GC-NS-Anodes, stable Mg metal deposition/stripping cycling was maintained during 1000 cycles with high average CEs of ~99.9% (Figure 2e). After the long-term cycling process, the carbon structure of GC-NS is well-maintained (Figure S4). In contrast, the Mo-Anode showed large fluctuations of the CE values after approximately 300 cycles, which lasted for ~450 cycles with a relatively low average CE of ~99.6%.

To compare the electrochemical performance of the GC-NS-Anode with other metal-based anodes (Mo, Cu, SS, and Mg), they were assembled into 2032-type coin cells and the same amount of Mg (0.5 mA h g^{-1}) was deposited electrochemically on them (Figure 3). In the galvanostatic Mg metal deposition profile, the initial overshooting voltage of the GC-NS-Anode (0.20 V, Figure 3a) was lower than those of the other types of substrates (Mo: 0.37 V; Cu: 0.53 V; SS: 0.43 V) and even lower than that of the Mg–Mg symmetric cell (0.49 V in Figure 3e). The appearance of polarization, including the initial shooting voltage and plateau overpotential,

which is indicated by the blue line, highlights the superior kinetic performance of the GC-NS-Anode for the deposition Mg ions. Interestingly, the GC-NS-Anode showed better accessibility and superior ability to accommodate Mg ions than the other types of substrates. The inset in Figure 3 presents images of the cell components of Mg metal, GF, and the substrates after deposition. The images of the ex-situ cell with the GC-NS-Anode revealed a clean GF separator (Figure 3a), whereas the GF separators of the other ex-situ cells with metal-based anodes were stained by deposited Mg metal (Figure 3b–d). In all metal-based substrates, most of the deposited Mg metal was stuck to the GF separator, which means that the direct growth of Mg metal on the substrate surface is unfavorable. Even in the case of the Mg–Mg symmetric cell (Figure 3e), Mg^{2+} ions deposited preferentially in the GF separator instead of the Mg anode. The Mg metal deposition behavior on the separator was also observed, when a relatively thin and dense polypropylene (PP) separator was used (Figure 3f). The poor wettability for the newly deposited Mg metal was recently discussed and highlighted as a crucial problem in the current RMBs.[17] The unwanted metal deposition in the nonconducting separators can deteriorate the CEs and cycling performances of RMBs significantly by clogging the separators. In this regard, the favorable Mg metal deposition on GC-NS-Anodes can explain why it could deliver improved CEs and cyclabilities, as shown in Figure 2d,e. XRD and scanning electron microscopy (SEM) were performed to examine as to where the electrochemically deposited Mg metal was located (Figures S5 and S6). In the case of the Mo-Anode, ex-situ XRD revealed the absence of Mg on the anode. Instead, the GF separator contained most of the electrochemically deposited Mg metals (Figure S5), demonstrating the seriousness of unfavorable metal deposition. In contrast, the ex-situ XRD pattern of the GC-NS-Anode showed the characteristic Mg peaks, indicating the major presence of Mg metal on the

anode (Figure S5a), and its absence on the GF separator was also confirmed (Figure S5d−f). Furthermore, ex-situ FE-SEM analysis showed that the GC-NSs contained and attached the electrochemically formed Mg in the macropores (Figure S7), demonstrating the superiority of GC-NSs as a template for accommodating Mg metal. Although Mo-, Cu-, and SS-based metal anodes have been used in previous studies, the effects on Mg metal deposition have not been of major interest. This result illustrates the unwanted Mg metal deposition behaviors on the separator.

To investigate the origin of the favorable Mg metal deposition on GC-NSs, the affinity (i.e., absorption energy) for Mg^{2+} ions at the graphene edges for GC-NSs was calculated using first-principles calculations and compared with Cu, Mo, and Mg substrates (Figure 4). The graphene sheets, where the edges are terminated with hydrogen atoms and heteroatoms, were designed, and the Mg atom was attached to the edge and fully relaxed. After considering the various bonding configurations, the most feasible absorption sites for Mg were confirmed to be the edge sites, where they neighbor with two oxygen atoms, exhibiting the highest chemisorption energy (−1.06 eV) (Figure 4a). In addition, absorption at the oxygen-terminated edges is more preferred than that on the basal plane of graphene (Figure S8). A perfect graphene sheet without a defect would be thermodynamically inactive for accepting Mg (1.48 eV in Figure S8a), and even in the case of defective graphene, the absorption energy (−0.45 eV in Figure S8b) is relatively lower than that on the active edge sites. To describe the defective phase, graphene with a monovacancy was chosen as a case study because it was demonstrated to be the most feasible site for Na ion absorption among the various vacancy types because of the large defect sites.[24] Considering that GC-NSs have numerous catalytic carbon edges bonded to oxygen heteroatoms, as shown experimentally in Figure 1a,e, favorable absorption could occur while the absorption energies onto Mo (−0.46 eV) and Cu (−0.28 eV) were relatively low (Figure 4b,c). In particular, absorption on Mg metal (0.67 eV, Figure 4d) is thermodynamically unfavorable, which would be the origin for the poor adhesion, as reported recently.[17,18] Notably, the calculations were well-matched with the experiment results of the adhesion test (Figure 3). Although the calculation results could present a few feasible cases and only the lowest surface energy slabs of Cu, Mo, and Mg were considered, the results clearly show that the affinity of Mg depends on the substrate types, which should be considered when designing efficient RMBs. Moreover, the numerous catalytic edges of GC-NSs were highly advantageous for accommodating Mg ions in the structure.

The full-cell test of the GC-NS-Anode demonstrates its feasibility as a stable and efficient anode for rechargeable Mg batteries (Figure S9). The successful synthesis of Chevrel-phase Mo_6S_8 was demonstrated by X-ray diffraction (XRD), and the spectrum is shown in Figure S9a. The full-cell was predeposited with Mg to 5 mAh in the anode/separator/Mg metal half-cells. The anodes were then reassembled into full-cells (each composed of anode/new separator/Mo_6S_8). As shown in Figure S9b, the discharge−charge property of the GC-NS full-cell (blue line) was highly stable. Meanwhile, the full-cell configured as Mo-anode/new separator/Mo_6S_8 shows poor capacity (red line, Figure S9b) because most of the deposited Mg ions in the Mo-anode half-cell were clogged in the separator (see Figure 3). This result demonstrates that Mg metal deposited on GC-NS-Anode works as the anode of a

rechargeable Mg battery, whereas Mg-deposited Mo cannot function as the anode.

■ CONCLUSIONS

In summary, we demonstrated that a well-designed GC-NS plays an important role in the electrochemical Mg metal deposition/stripping performance of Mg metal anodes (MMAs) for RMBs. The performance of the fabricated GC-NS greatly surpassed those of conventional metal substrate-based anodes. In a galvanostatic Mg metal deposition process, the initial nucleation overpotential (η_n) and plateau over-potential (η_p) were reduced significantly with GC-NSs compared to those of the Mo-Anode. In addition, the VO and overpotential gaps between GC-NS-Anode and Mo-Anode increased gradually with increasing current density, indicating high rate capabilities for the GC-NS-Anode. One of the most noteworthy results revealed significantly improved CEs and cycling stabilities in the GC-NS-Anode. The ex situ experimental results and density functional theory (DFT) data showed that Mg^{2+} ions have high affinity to GC-NSs, leading to favorable Mg metal deposition in the targeted macropores. In contrast, metal-based substrates, which are used conventionally in RMBs, show a relatively poor affinity to Mg^{2+} ions, exhibiting unwanted Mg metal deposition behaviors on the GF and PP separators. These results showed that catalytic carbon nanotemplates rather than conventional metal-based substrates are essential to achieving high-performance RMBs.

■ EXPERIMENTAL SECTION

Preparation of GC-NSs. Bacterial cellulose pellicles (BCPs) were cultivated from *Gluconacetobacter xylinum* using a reported procedure.[25] Briefly, the cells were precultured in a test tube for 1 week and then inoculated into a Petri dish containing Hestrin and Schramm medium. The cells in the Petri dish were incubated statically at room temperature for 1 week. The BCPs were purified in a 0.25 M NaOH aqueous solution for 48 h at room temperature to eliminate the cells and components of the culture liquid. The BCPs were washed thoroughly with distilled water until the pH reached 7.0. The cultivated BCPs were immersed in tert-butanol for solvent exchange for 6 h and then freeze-dried at −40 °C and ∼5 Pa for 3 days. The resulting cryogel was treated thermally in a tube-furnace at 800 °C for 2 h under a N_2 gas flow of 200 mL min^{-1}. The carbonized sample was then heated in a graphite furnace (ThermVac, Korea) to 2800 °C for 2 h under an Ar atmosphere, where a heating rate of 5 °C min^{-1} was applied. The product, GC-NSs, was used without further treatment as a substrate for Mg metal storage.

Characterization. X-ray diffraction (XRD, Rigaku, MiniFlex) with Cu Kα radiation was used to analyze the crystal structures of the products after the electrochemical test, and their morphologies were observed by field-emission scanning electron microscopy (FE-SEM, FEI, Inspect F) and field-emission transmission electron microscopy (FE-TEM, JEM2100F, JEOL, Japan). The Raman spectra of the samples were recorded using a continuous-wave linearly polarized laser (532 nm, 2.41 eV, 16 mW). The laser beam was focused by a 100× objective lens, resulting in a spot diameter of ∼1 μm. The acquisition time and number of cycles to collect each spectrum were 10 s and 3, respectively. The chemical composition and depth profile were examined by XPS (PHI 5700 ESCA, Chanhassen) using monochromatic Al Kα radiation. The electrical conductivity of the GC-NSs was tested using an electrical conductivity meter (Loresta GP, Mitsubishi Chemical, Japan). The porous properties of the GC-NSs were analyzed by nitrogen adsorption and desorption isotherms obtained using a surface area analyzer and a porosimetry analyzer (ASAP 2020, Micromeritics) at −196 °C. The electrochemical cells for the Mg batteries were assembled into 2032-type coin cells in an

argon-filled glovebox (<1 ppm O_2 and <1 ppm H_2O). All of the cell components were washed prior to use and prepared carefully without exposure to air. The scratched Mg metal disk (99.95% metals basis, Alfa Aesar) was assembled into a coin cell as quickly as possible in an argon-filled glovebox. All-phenyl complex (APC) electrolytes were prepared by mixing 0.5 M $AlCl_3$ and 2.0 M PhMgCl in a tetrahydrofuran (THF) solvent, which was maintained with a molecular sieve (4 Å) to remove the residual water (<10 ppm measured by the Karl−Fischer coulometer, Metrohm). To prepare the substrate for reversible Mg metal storage, the GC-NS material was punched into cylinders of 1/2 in diameter. These cylinders were used as the working electrodes without active material (Mg metal) in the half-cell test. Mg metal was deposited on the metal-free GC-NSs (substrate) during the discharge process, and was fully dissolved during the charge process. The pristine working electrode without active material (GC-NCs) in the half-cell is simply named the "anode". In addition, the CE was calculated from the discharge/charge cycles on the metal-free GC-NSs anode. In the full-cell system, the Chevrel-phase Mo_6S_8 cathode material cannot source Mg, and so Mg metal was predeposited to 5 mAh on GC-NC in the GC-NS/separator/Mg metal half-cell. The metal-deposited GC-NC-Anode was then dissembled and reassembled into a full-cell configured as GC-NS-Anodes/new separator/Mo_6S_8. The electrochemical properties measured using a potentio-galvanostat (WonA Tech, WBCS 3000) and the capacities were calculated based on the area of the substrates.

Calculation Details. All calculations were performed using density functional theory (DFT) as implemented in the Vienna Ab initio Simulation Package.[26] The DFT calculations were based on the projector augmented wave method.[27,28] The Perdew−Burke−Ernzerhof-generalized gradient approximation was used for the exchange-correlation energy functional.[29] An energy cut off of 500 eV was used for the plane wave basis set. The convergence criterion for the electronic self-consistency loop was 10^{-5} eV, and the atomic positions were relaxed until the forces were less than 0.03 eV Å^{-1}. The optimal lattice parameters of the bulk system were obtained by fitting the energy versus volume to the Murnaghan equation of state.[30] The lowest surface energy slabs, Mg(0001), Cu(111), and Mo(110), were used for the calculation.[31] Supercells were generated to minimize the effects of periodic Mg atoms, increasing the number of atoms to 64, 64, 96, and 72 for Mg, Cu, Mo, and graphene slabs, respectively. The graphene sheets with a monovacancy and oxygen termination were obtained from the previous reports.[24,32] A vacuum layer of 25 Å was included in the supercells and the calculations employed γ-centered grids with a $2 \times 2 \times 1$ mesh. Ionic relaxation was performed for all atoms, whereas the back two layers were fixed for Mg, Cu, and Mo slabs for their bulk-like positions. The Mg adsorption energy, E_{ad}, was evaluated as $E_{ad} = E_{total} - E_{substrate} - E_{Mg}$, where E_{total}, $E_{substrate}$, and E_{Mg} are the total energies of the entire system, substrate, and metallic Mg, respectively.

ASSOCIATED CONTENT

Ⓢ Supporting Information

The Supporting Information is available free of charge on the ACS Publications website at DOI: 10.1021/acsami.9b13447.

Surface topography data, optical images, ex-situ FE-SEM images, and electrochemical results (PDF)

AUTHOR INFORMATION

Corresponding Authors
*E-mail: hdlim@kist.re.kr (H.-D.L).
*E-mail: c-ysyun@korea.ac.kr (Y.S.Y.).

ORCID Ⓘ
Hyoung-Joon Jin: 0000-0002-1763-9455
Si Hyoung Oh: 0000-0002-7063-9235
Young Soo Yun: 0000-0002-2937-9638

REFERENCES

(1) Yoo, H. D.; Shterenberg, I.; Gofer, Y.; Gershinsky, G.; Pour, N.; Aurbach, D. Mg rechargeable batteries: an on-going challenge. *Energy Environ. Sci.* **2013**, *6*, 2265−2279.

(2) Tutusaus, O.; Mohtadi, R.; Singh, N.; Arthur, T. S.; Mizuno, F. Study of Electrochemical Phenomena Observed at the Mg Metal/Electrolyte Interface. *ACS Energy Lett.* **2017**, *2*, 224−229.

(3) Robba, A.; Vizintin, A.; Bitenc, J.; Mali, G.; Arčon, I.; Kavčič, M.; Žitnik, M.; Bučar, K.; Aquilanti, G.; Martineau-Corcos, C.; Randon-Vitanova, A.; Dominko, R. Mechanistic Study of Magnesium−Sulfur Batteries. *Chem. Mater.* **2017**, *29*, 9555−9564.

(4) Muldoon, J.; Bucur, C. B.; Gregory, T. Quest for nonaqueous multivalent secondary batteries: magnesium and beyond. *Chem. Rev.* **2014**, *114*, 11683−11720.

(5) Zhang, Z.; Dong, S.; Cui, Z.; Du, A.; Li, G.; Cui, G. Rechargeable Magnesium Batteries using Conversion-Type Cathodes: A Perspective and Minireview. *Small Methods* **2018**, *2*, No. 1800020.

(6) Song, J.; Sahadeo, E.; Noked, M.; Lee, S. B. Mapping the challenges of magnesium battery. *J. Phys. Chem. Lett.* **2016**, *7*, 1736−1749.

(7) Lu, Z.; Schechter, A.; Moshkovich, M.; Aurbach, D. On the electrochemical behavior of magnesium electrodes in polar aprotic electrolyte solutions. *J. Electroanal. Chem.* **1999**, *466*, 203−217.

(8) Gregory, T. D.; Hoffman, R. J.; Winterton, R. C. Nonaqueous Electrochemistry of Magnesium: Applications to Energy Storage. *J. Electrochem. Soc.* **1990**, *137*, 775−780.

(9) Shterenberg, I.; Salama, M.; Yoo, H. D.; Gofer, Y.; Park, J.-B.; Sun, Y.-K.; Aurbach, D. Evaluation of (CF3SO2) 2N−(TFSI) based electrolyte solutions for Mg batteries. *J. Electrochem. Soc.* **2015**, *162*, A7118−A7128.

(10) Ma, Z.; Kar, M.; Xiao, C.; Forsyth, M.; MacFarlane, D. R. Electrochemical cycling of Mg in Mg[TFSI]2/tetraglyme electrolytes. *Electrochem. Commun.* **2017**, *78*, 29−32.

(11) Gaddum, L.; French, H. The electrolysis of grignard solutions1. *J. Am. Chem. Soc.* **1927**, *49*, 1295−1299.

(12) Connor, J. H.; Reid, W. E.; Wood, G. B. Electrodeposition of Metals from Organic Solutions: V. Electrodeposition of Magnesium and Magnesium Alloys. *J. Electrochem. Soc.* **1957**, *104*, 38−41.

(13) Aurbach, D.; Lu, Z.; Schechter, A.; Gofer, Y.; Gizbar, H.; Turgeman, R.; Cohen, Y.; Moshkovich, M.; Levi, E. Prototype systems for rechargeable magnesium batteries. *Nature* **2000**, *407*, 724.

(14) Keyzer, E. N.; Glass, H. F.; Liu, Z.; Bayley, P. M.; Dutton, S. E.; Grey, C. P.; Wright, D. S. Mg(PF6)2-based electrolyte systems: understanding electrolyte−electrode interactions for the development of mg-ion batteries. *J. Am. Chem. Soc.* **2016**, *138*, 8682−8685.

(15) Ha, J. H.; Cho, J.-H.; Kim, J. H.; Cho, B. W.; Oh, S. H. 1-Butyl-1-methylpyrrolidinium chloride as an effective corrosion inhibitor for stainless steel current collectors in magnesium chloride complex electrolytes. *J. Power Sources* **2017**, *355*, 90−97.

(16) Son, S.-B.; Gao, T.; Harvey, S. P.; Steirer, K. X.; Stokes, A.; Norman, A.; Wang, C.; Cresce, A.; Xu, K.; Ban, C. An artificial interphase enables reversible magnesium chemistry in carbonate electrolytes. *Nat. Chem.* **2018**, *10*, 532.

(17) Ding, M. S.; Diemant, T.; Behm, R. J.; Passerini, S.; Giffin, G. A. Dendrite growth in Mg metal cells containing Mg (TFSI)2/glyme electrolytes. *J. Electrochem. Soc.* **2018**, *165*, A1983−A1990.

(18) Davidson, R.; Verma, A.; Santos, D.; Hao, F.; Fincher, C.; Xiang, S.; Buskirk, J. V.; Xie, K.; Pharr, M.; Mukherjee, P. P.; Banerjee, S. Formation of Magnesium Dendrites during Electrodeposition. *ACS Energy Lett.* **2018**, *4*, 375−376.

(19) Tan, Y.-H.; Yao, W.-T.; Zhang, T.; Ma, T.; Lu, L.-L.; Zhou, F.; Yao, H.-B.; Yu, S.-H. High Voltage Magnesium-ion Battery Enabled by Nanocluster Mg_3Bi_2 Alloy Anode in Noncorrosive Electrolyte. *ACS Nano* **2018**, *12*, 5856−5865.

(20) Zhang, Y.; Geng, H.; Wei, W.; Ma, J.; Chen, L.; Li, C. C. Challenges and recent progress in the design of advanced electrode materials for rechargeable Mg batteries. *Energy Storage Mater.* **2019**, *20*, 118−138.

(21) Hattori, M.; Yamamoto, K.; Matsui, M.; Nakanishi, K.; Mandai, T.; Choudhary, A.; Tateyama, Y.; Sodeyama, K.; Uchiyama, T.; Orikasa, Y.; Tamenori, Y.; Takeguchi, T.; Kanamura, K.; Uchimoto, Y. Role of Coordination Structure of Magnesium Ions on Charge and Discharge Behavior of Magnesium Alloy Electrode. *J. Phys. Chem. C* **2018**, *122*, 25204−25210.

(22) Song, M.; Niu, J.; Yin, K.; Gao, H.; Zhang, C.; Ma, W.; Luo, F.; Peng, Z.; Zhang, Z. Self-supporting, eutectic-like, nanoporous biphase bismuth-tin film for high-performance magnesium storage. *Nano Res.* **2019**, *12*, 801−808.

(23) Pei, A.; Zheng, G.; Shi, F.; Li, Y.; Cui, Y. Nanoscale Nucleation and Growth of Electrodeposited Lithium Metal. *Nano Lett.* **2017**, *17*, 1132−1139.

(24) Yun, Y. S.; Park, K. Y.; Lee, B.; Cho, S. Y.; Park, Y. U.; Hong, S. J.; Kim, B. H.; Gwon, H.; Kim, H.; Lee, S.; Park, Y. W.; Jin, H.-J.; Kang, K. Sodium-ion storage in pyroprotein-based carbon nanoplates. *Adv. Mater.* **2015**, *27*, 6914−6921.

(25) Yun, Y. S.; Bak, H.; Jin, H.-J. Porous carbon nanotube electrodes supported by natural polymeric membranes for PEMFC. *Synth. Met.* **2010**, *160*, 561−565.

(26) Kresse, G.; Furthmüller, J. Efficient iterative schemes for ab initio total-energy calculations using a plane-wave basis set. *Phys. Rev. B* **1996**, *54*, No. 11169.

(27) Blöchl, P. E. Projector augmented-wave method. *Phys. Rev. B* **1994**, *50*, No. 17953.

(28) Kresse, G.; Joubert, D. From ultrasoft pseudopotentials to the projector augmented-wave method. *Phys. Rev. B* **1999**, *59*, No. 1758.

(29) Perdew, J. P.; Burke, K.; Ernzerhof, M. Generalized gradient approximation made simple. *Phys. Rev. Lett.* **1996**, *77*, No. 3865.

(30) Murnaghan, F. The compressibility of media under extreme pressures. *Proc. Natl. Acad. Sci. U.S.A.* **1944**, *30*, 244.

(31) Tran, R.; Xu, Z.; Radhakrishnan, B.; Winston, D.; Sun, W.; Persson, K. A.; Ong, S. P. Surface energies of elemental crystals. *Sci. Data* **2016**, *3*, No. 160080.

(32) Yun, Y. S.; Kim, D.-H.; Hong, S. J.; Park, M. H.; Park, Y. W.; Kim, B.; Jin, H.-J.; Kang, K. Microporous carbon nanosheets with redox-active heteroatoms for pseudocapacitive charge storage. *Nanoscale* **2015**, *7*, 15051−15058.